Lowering the Operating Temperature of Perovskite Catalysts for N_2O Decomposition Through Control of Preparation Methods

Nia Richards,[1] James H. Carter,[1] Luke A. Parker,[1,2] Samuel Pattisson,[1] Daniel G. Hewes,[1] David J. Morgan,[1] Thomas E. Davies,[1] Nicholas F. Dummer,[1] Stanislaw Golunski,[1] Graham J. Hutchings[1]*

[1]Cardiff Catalysis Institute, School of Chemistry, Cardiff University, Cardiff, CF10 3AT UK

[2]Now at; Inorganic Chemistry and Catalysis Debye Institute for Nanomaterials Science, Utrecht University, Universiteitsweg 99, 3584CG Utrecht (The Netherlands)

*Corresponding author: Hutch@cardiff.ac.uk

Abstract

Discovering catalysts that can decompose N_2O at low temperatures represents a major challenge in modern catalysis. The effect of preparative route on N_2O-decomposition activity has been examined for a $PrBaCoO_3$ perovskite catalyst. Initially, a citric acid preparation was utilised where the A site ratio was altered in order to increase phase purity. Comparable compositions were then prepared by an oxalic acid precipitation method and by a supercritical anti-solvent technique to produce perovskites with a higher surface area (> 30 m^2g^{-1}). By altering the A site ratio it was possible to reduce the temperature required to produce a pure phase perovskite whilst maintaining a higher-surface area. The use of the different preparation methods resulted in perovskites with varying properties, as determined by N_2 adsorption, XPS, O_2-TPD and H_2-TPR. This work confirms the importance of lattice oxygen species that have high oxygen mobility for enhanced decomposition of N_2O, as oxygen recombination is considered the rate-limiting step. Here, the formation of molecular oxygen is limited by surface adsorbed O species being within a distance at which oxygen recombination is possible. The most active PrBaCo-based catalyst did not have the highest percentage of lattice oxygen as shown by XPS, however, the catalytic activity could be correlated to the mobile oxygen species and high surface area. The PrBaCo-based catalyst prepared by supercritical anti-solvent converted 50 % of the N_2O present in the feed (T_{50}) at 410 °C, which represents a significant improvement over reported catalytic performance measured under similar conditions.

Keywords: Perovskites, Supercritical Anti-Solvent, Nitrous Oxide Decomposition, Oxygen Vacancies, Mobile Lattice Oxygen, Surface Area.

Introduction

Although it accounts for only 315 ppb of the atmosphere, nitrous oxide (N_2O) has disproportionately large detrimental effects on the environment. As well as being a highly potent greenhouse gas, as shown by its global warming potential of being *ca*. 300 times more detrimental when compared CO_2,[1–3] it has an ozone depletion potential comparable to many HCFCs. Global N_2O emissions are generated largely (ca. 60%) via anthropogenic activities and originate from industrial chemical processes such as adipic acid production, sewage treatment, the agriculture sector or combustion sources (stationary and mobile).[4–8] Alongside large scale industrial sources, there are numerous smaller unregulated emissions such as those from hospitals, dental surgeries and veterinary practices where N_2O is used as an anaesthetic and analgesic.[9] Consequently, the development of catalysts that can efficiently decompose N_2O (Eq. 1) is of great importance:

$$2\ N_2O \rightarrow 2\ N_2 + O_2 \qquad (\Delta_rH^o\ (298\ K) = -163\ kJmol^{-1})\ [10] \qquad (Eq.\ 1)$$
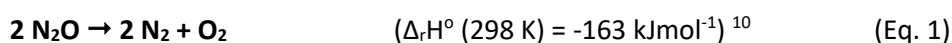
There are many existing catalysts that can be used for N_2O decomposition including ceria-based materials,[11–13] spinels [14–16] and supported metals.[17–21] Perovskites are a well-known class of materials represented by the formula ABO_3, with the A site generally being a large, rare earth element such as La. The B site is typically a smaller transition metal element such as Co or Fe. The substitution of elements into the A or B site leads to the formation of varied valencies of redox couples on the B site cation, which results in the formation of oxygen vacancies. Sr or Ce are often used for A site substitution.[10] Perovskites are known for their low cost and high structural and thermal stability, which usually arises due to the high temperatures required to form the perovskite phase.[22–26] This high temperature preparation leads to low specific surface areas, typically less than 10 $m^2\ g^{-1}$.[10,22,27–30] There has been a significant effort to produce perovskites with high surface area. [31–34] Interest in the preparation and use of perovskites has increased significantly in recent years due to the use of perovskites as solar cells, [35–40] with perovskites now showing comparable results to commercial solar cells. [41] Perovskites are also known for their oxygen mobility, ease of oxygen vacancy formation and oxygen storage capacity, with these factors contributing greatly to their high catalytic activity for N_2O decomposition.[42–45] The most notable perovskite catalysts for N_2O decomposition are given in Table 1. Manipulation of the oxidation state of the A and B site metals produces discrepancies in the ABO_3 structure resulting in an oxygen vacancy. For example, an A^{3+} cation can be substituted by an A^{2+} cation. Oxygen vacancies can provide adsorption sites for reactants and subsequent activation can take place, hence their presence in the perovskite structure can be directly linked to their catalytic activity.[46] As shown in Table 1, the surface area of these catalysts is just $1 – 12\ m^2g^{-1}$, which limits the productivity of the catalyst. A preparation method that can yield high surface area (> 30 m^2g^{-1})

perovskites would lead to a significant advance in the performance of perovskites for many applications beyond a catalyst.

The supercritical anti-solvent (SAS) precipitation preparation method is novel method that has been shown to yield nano-sized crystallites, which often result in high surface area materials compared to conventional techniques.[34,47–49] The origin of the high surface area in perovskites is the small primary particle size that is formed during the preparation, which is typically in the order of nanometres. Additionally, the precipitate is dried under supercritical CO_2 and the solvent is extracted, not evaporated. The effect of this is to minimise any pore collapse that can otherwise occur when water or other solvents are evaporated from the surface of porous solids. Additionally, the precursor formed in the SAS preparation are typically a carbonate or hydroxycarbonate. In contrast to a bulky organic ligand, a hydroxycarbonate would be expected to be decompose/combust at a lower energy and thus reduce this exothermic event through thermal treatment. Both citric acid preparation and oxalic acid preparation are sol-gel techniques that make use of bulky organic precursors, which lead to an increased exothermic decomposition and likely sintering. [25,50–53]

Table 1. Table showing the most relevant perovskites for N_2O decomposition.

Perovskite	Conditions	Conversion and T_{50}[a]	Specific Surface Area (m^2g^{-1})	Reference
$LaCoO_3$	0.5 % N_2O, He, WHSV = 120 000 mL g^{-1} h^{-1}	100 % at 550 °C T_{50} at 455 °C	7.7	54
$Pr_{0.8}Ba_{0.2}MnO_3$	0.5 g, 0.5 % N_2O, He balance. GHSV = 7500 h^{-1}	100 % at 550 °C T_{50} at 442 °C	12	55
$La_{0.7}Ba_{0.3}Mn_{0.8}In_{0.2}O_3$	10 % N_2O in He, 20 ml min^{-1} W/F = 3.0 g s cm^{-3}	92 % at 500 °C T_{50} at 443 °C	8	56
$La_{0.7}Sr_{0.3}MnO_3$	0.15 % N_2O GHSV = 30 800 h^{-1}	T_{50} at 725 °C	4.1	57,58
$La_{0.4}Sr_{0.6}FeO_3$	0.15 % N_2O Contact time 5 $x10^{-4}$ s	T_{50} at 815 °C	1	59

[a] Temperature required to achieve 50 % N_2O conversion

As shown in Table 1 various perovskites have been reported to be effective catalysts for the decomposition of N_2O at higher temperatures. For example, Russo *et al.* prepared a $LaCoO_3$ perovskite by a solution combustion synthesis method and reported 100 % conversion of 0.5 % N_2O in He at 550 °C, with a T_{50} of 455 °C.[54] Ivanov and co-workers prepared a series of $LaSrMnO_3$ catalysts, investigating the effects of the ratio of La and Sr in the A site. The optimal ratio was found to be $La_{0.75}Sr_{0.25}$, with a T_{50} of 725 °C under conditions of 0.15 % N_2O, and a contact time 5 $x10^{-4}$ s.[57,58] The

effect of doping on the oxygen mobility in $La_{0.4}Sr_{0.6}FeO_3$ catalysts was later studied. $La_{0.4}Sr_{0.6}FeO_3$ decorated with *ca.* 10 wt. % $LaSrFeO_4$ increased the activity of the catalyst compared with the as-prepared perovskite. The high activity was attributed to the increased oxygen lattice exchange and oxygen mobility, underlining this as a key parameter for active N_2O decomposition catalysts.[59]

Takita and co-workers investigated the effect of multiple A and B site compositions on the decomposition of N_2O using a $LaBaMnInO_3$ catalytic system. $La_{0.7}Ba_{0.3}Mn_{0.8}In_{0.2}O_3$ was the most active catalyst with a T_{50} at 443 °C over 10 % N_2O in He at 20 ml min^{-1}.[56] Kumar and co-workers reported a similar T_{50} by preparing a $Pr_{0.8}Ba_{0.2}MnO_3$ catalyst, initially by co-precipitation and then impregnation. They achieved 100 % conversion at 550 °C over 0.5 % N_2O/He and a GHSV of 7500 h^{-1}.[55] The high activity correlated to the enhanced redox properties associated with the Mn^{4+}/Mn^{3+} ratio and the corresponding charge compensation effect via substitution of Ba into the A site. The catalyst prepared by Kumar and co-workers are amongst the most active perovskites for N_2O decomposition reported to date, although the reaction conditions favour a high conversion of N_2O. The reactions are performed with a low concentration of N_2O (0.5 %) and at low GSHV (7500 h^{-1}) resulting in a high contact time. This is even more evident when calculating the space time yield, at 450 °C, a conversion of 69 % results in a space time yield of 1.2 mol h^{-1} kg^{-1}.

In this work, we investigate the influence of the A (PrBa) site metal ratio in an $PrBaCoO_3$ perovskite and prepare the catalyst by different methods in an attempt to increase the surface area and the oxygen mobility, and hence lower the operating temperature. Changing the A site ratio from 1:1 to 3:1 increased the purity, leading to a lowering of the temperature of formation for perovskites. This produced catalysts with higher surface areas and consequently higher catalytic activity, (T_{50} decreased from 527 °C to 445 °C). The use of an innovative preparation method in supercritical anti-solvent precipitation led to the formation of a perovskite with a specific surface area of 30 m^2 g^{-1} and a high oxygen mobility which led to a T_{50} of 410 °C. This is significantly lower than the most active literature catalyst (T_{50} 442 °C [55]), despite the drastically different conditions, 0.0625 g of catalyst compared to 0.5 g and a N_2O concentration of double that are used in literature. Therefore, an improvement of 32 °C in the T_{50} over the past 7 years is a drastic improvement in what is still an important global topic, N_2O abatement.

Experimental

Catalyst Preparation

Citric Acid Preparation: Benchmark perovskite based catalysts were prepared by citric acid preparation as described by Fierro *et al.*[25,50] Metal nitrates dissolved in deionised water (50 mL) while stirring at 50 °C in a round bottom flask. Citric acid (Sigma Aldrich, > 99.95 %) (metal:citric acid = 1:2 molar ratio) was added to the solution and the temperature increased to 90 °C. After 30 min the temperature was further increased to 110 °C and left under stirring for 16 h, which yielded a dry powder. Following grinding, all catalysts were pre-treated in an oven at > 200 °C with a ramp rate of 1 °C min^{-1} to pass the point of citric acid combustion, as indicated by TGA. Finally, the materials were calcined in flowing air at a suitable temperature, for 3 hours at 1 °C min^{-1} to form a pure phase perovskite, as determined by in-situ X-ray diffraction (XRD)

Oxalic Acid Preparation: Perovskite catalysts with enhanced phase purity were prepared using oxalic acid as a precipitation agent, based on the work by Fan *et al.*[51–53] Metal nitrates were added in the appropriate ratios totalling 0.02 moles of metal to ethanol (200 mL, Sigma Aldrich, 99.8 %) and stirred. Once the metal salts were dissolved, oxalic acid (0.024 moles, Sigma Aldrich, > 99 %) was added and the solution was left to age for 2 h at room temperature. After aging the solution was filtered and washed with ethanol (500 mL) and dried in oven at 110 °C for 16 h. The resulting solid was pre-treated in a chamber oven at 300 °C, followed by calcination in flowing air at a suitable temperature to form a pure phase perovskite, as determined by *in situ* XRD.

Supercritical Anti-Solvent (SAS) Preparation: High surface area perovskite catalysts were prepared using the supercritical anti-solvent (SAS) precipitation method. A brief summary of the preparation method is given below with more detailed experimental method including a technical diagram previously reported.[34,47,60,61] A mixture of metal acetylacetone hydrate and acetate precursor salts were dissolved in ethanol (Sigma Aldrich 99.8 %) with 5 % deionised water. SAS experiments were performed using apparatus manufactured by Separex. CO_2 (99.99 %, BOC) was pumped through the system (held at 150 bar, 40 °C) via the outer part of a co-axial nozzle at a rate of 12 kg h^{-1} (41 Hz). The metal salt solution was concurrently pumped through the inner nozzle using an Agilent HPLC pump at a rate of 4 mL min^{-1}. At this point, the solvent rapidly solubilises into the surrounding supercritical CO_2, causing the precipitation of the metal precursors. This was recovered on a stainless-steel frit, while the CO_2–solvent mixture passed down stream, where the pressure was decreased to separate the solvent and CO_2. Precipitation was carried out for 120 min followed by a purge of the system with CO_2 for 1 h under 150 bar and 40 °C. The system was then depressurised, and the dry powder collected. The resulting SAS precipitates were then pre-treated in a chamber oven at 300 °C, followed by

calination in flowing air at a suitable temperature to form a pure phase perovskite, as determined by *in situ* XRD.

N₂O decomposition

All reactions were performed at atmospheric pressure in a continuous-flow fixed-bed reactor. A reactor tube (4.6 mm internal diameter, stainless steel) was packed with catalyst (0.0625 g) between two layers of quartz wool. Reactions were performed over the temperature range of 200 – 600 °C, with a flow rate of 100 ml min^{-1} (GHSV: PBC CA 33 000 h^{-1}, PBC OA 37000 h^{-1}, PBC SAS 38000 h^{-1}, BPC CA 47 000 h^{-1}). The gas feed was composed of 1 % N₂O in He. All outgoing gaseous products were analysed online using an Agilent 7890B Gas Chromatograph (GC) (columns: Hayesep Q (80-100 mesh, 1.8 m) MolSieve 5A (80-100 mesh, 2 m) fitted with a thermal conductivity detector.

N₂O decomposition rate (mol$_{N2O}$ h^{-1} kg$_{cat}^{-1}$ shortened to mol h^{-1} kg^{-1}) is given by the equation:

$$\frac{Conversion\ at\ given\ temperature\ (\%)\ *\ Flow\ rate\ of\ N_2O\ (mol\ h^{-1})}{catlayst\ weight\ (kg)}$$

N₂O decomposition rate (mol$_{N2O}$ h^{-1} m^{-2} shortened to mol h^{-1} m^{-2}) is given by the equation:

$$\frac{Conversion\ at\ given\ temperature\ (\%)\ *\ Flow\ rate\ of\ N_2O\ (mol\ h^{-1})}{Catalyst\ surface\ area\ (m^2g^{-1})\ *\ catalytst\ weight\ (g)}$$

Catalyst Characterisation

X-ray photoelectron spectroscopy (XPS) was performed on a Thermo Fisher Scientific K-alpha$^+$ spectrometer. Samples were analysed using a micro-focused monochromatic Al X-ray source (72 W) over an area of approximately 400 microns. Data was recorded at pass energies of 150 eV for survey scans and 40 eV for high resolution scan with 1 eV and 0.1 eV step sizes respectively. Charge neutralisation of the sample was achieved using a combination of both low energy electrons and argon ions. Data analysis was performed in CasaXPS using a Shirley type background and Scofield cross sections, with an energy dependence of -0.6.

X-ray Diffraction (XRD) analysis was performed on a PANalytical X'Pert Pro diffractometer using a Ni-filtered CuKα radiation source operating at 40 KV and 40 mA. Standard analysis was performed using a 40 min run with a back filled sample holder. Patterns were identified using the International Centre for Diffraction Data Powder Diffraction File.

In-situ XRD was performed using a PANalytical X'Pert Pro diffractometer using a Ni-filtered CuKα radiation source operating at 40 KV and 40 mA, fitted with a cell that allows temperature control and gas flow using Bronkhorst mass flow controllers. Characterisation was controlled via software, the

'Data collector' program was used to set temperature, run time and repeats measurements. Patterns were identified using the International Centre for Diffraction Data Powder Diffraction File.

Thermogravimetric Analysis (TGA) was performed using a Perkin Elmer TGA 4000, with 10 mg sample with 50 mL min^{-1} air and a ramp rate of 5 °C min^{-1}, from 30 – 800 °C. Mass losses were recorded as changes in mg and converted into a percentage of the total mass of the sample. The metal nitrates used in this study were analysed to determine their decomposition temperatures, the mass loss profiles are shown in Fig. S1 a-h. These profiles are used to identify the mass loss events in the catalyst's profiles. Due to the ramp rate of 5 °C min^{-1} there is likely to be a delay of ± 20 °C to the final mass loss event when compared to a calcination that is held at a temperature.

Microwave Plasma Atomic Emission Spectroscopy (MP-AES) was performed using an Agilent 4100 MP-AES utilising Agilent MP expert software. Calibration samples were prepared by dilution of a standard metal solution with deionised water. A minimum of four calibration plots were used per analysis. Solid catalyst samples (50 mg) were dissolved in aqua regia (4 mL diluted to 50 mL with deionised water) to give a pre-calculated approximate metal concentration, followed by MP-AES analysis to give an accurate determination of the metal ratios.

Oxygen Temperature Programmed Desorption (O$_2$-TPD) profiles were performed using a ChemBET TPR/TPD equipped with a TCD to monitor oxygen evolution. A pre-treatment in He up to 550 °C was performed, followed by doping of oxygen using 10 %O$_2$/He at 550 $^{\circ}$C, the sample was cooled to room temperature and the gas changed to He, followed by desorption of oxygen up to 850 °C at 10 °C min^{-1} and held for 10 min at T$_{max}$, using an attenuation of 2, TCD sensitivity of 150 and flow 30 mL min^{-1}. The sample mass was typically 60 mg.

Nitrogen adsorption isotherms were collected using a Quantachrome Quadrasorb evo. A 20-point analysis was performed using N$_2$ as the adsorbate gas. Samples were degassed for 14 h at 300 °C prior to analysis. Analyses was carried out at -196 °C with P$_0$ measured continuously. Free space was measured post analysis with He. The data was analysed using the BET method.

SEM Microscopy was performed on a Tescan MAIA3 field emission gun scanning electron microscope (FEG-SEM) fitted with secondary and backscattered electron detection. Energy-dispersive X-ray (EDX) analysis and mapping was performed using an Oxford Instruments X-Max^{N}80 detector and the data analysed using the Aztec software. EDX analysis was performed using the Oxford Aztec Point and ID software. Samples were dry mounted on 300 mesh copper grids coated with holey carbon film.

TEM images and diffraction patterns were taken on a Jeol 2100JEM Transmission Electron Microscope. Samples were prepared on holey carbon copper grids (TAAB) and viewed via a single tilt holder. The

following magnifications were used to achieve the scale bars seen: 300 kx (20 nm scale bar), 600 kx (10 nm scale bar), 1 Mx (5 nm scale bar).

TPR was performed using a ChemBET TPR/TPD equipped with a TCD to monitor hydrogen uptake. A pre-treatment in He up to 150 $^{\circ}$C was performed, followed by a reduction in 10 %H_2/Ar up to 800 $^{\circ}$C, held for 30 min at T_{max}, using an attenuation of 4, TCD sensitivity of 150 and flow 15 mL min^{-1}. The sample mass used was typically between 40 – 50 mg.

Results and Discussion

BaPrCoO$_3$ (BPC) was prepared by the combination of citric acid and a mixture of metal nitrates, using a molar ratio of 2:1. Thermal analysis of BPC (Fig. 1 a) shows a sharp mass loss below 200 °C that can be associated to the decomposition of citric acid into CO$_2$. Further mass losses were recorded at 300 °C, due to the decomposition of Co nitrate and Ba nitrate, and a minor mass loss at 580 °C, due to the decomposition of Pr nitrate. To form the pure phase perovskite, the catalyst precursor was treated at a high temperature as determined by *in situ* XRD. When performing *in situ* XRD the sample must be packed into a sample holder, it is crucial that when the sample is heated the sample remains flat and the holder fully packed to ensure the incidence angle of the X-rays remain consistent. Therefore, the catalyst must be pre-treated to limit mass loss when obtaining *in situ* XRD patterns. For this catalyst, 400 °C was chosen as most major mass loss events had occurred below this point, with over 60 % catalyst mass lost (Fig. 1 a). Importantly all pre-treatments were performed at 1 °C min^{-1} in a chamber oven for 2 h to ensure that the exothermic reaction was safely controlled.
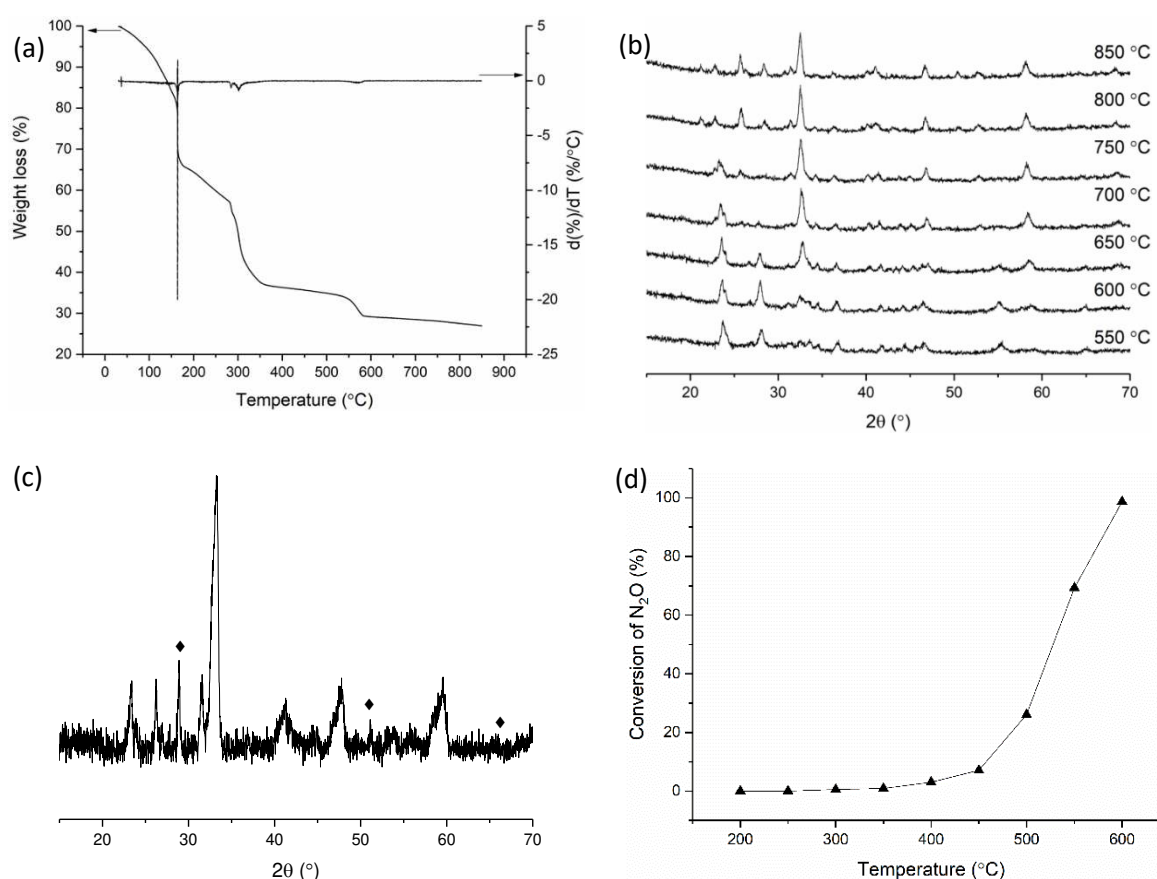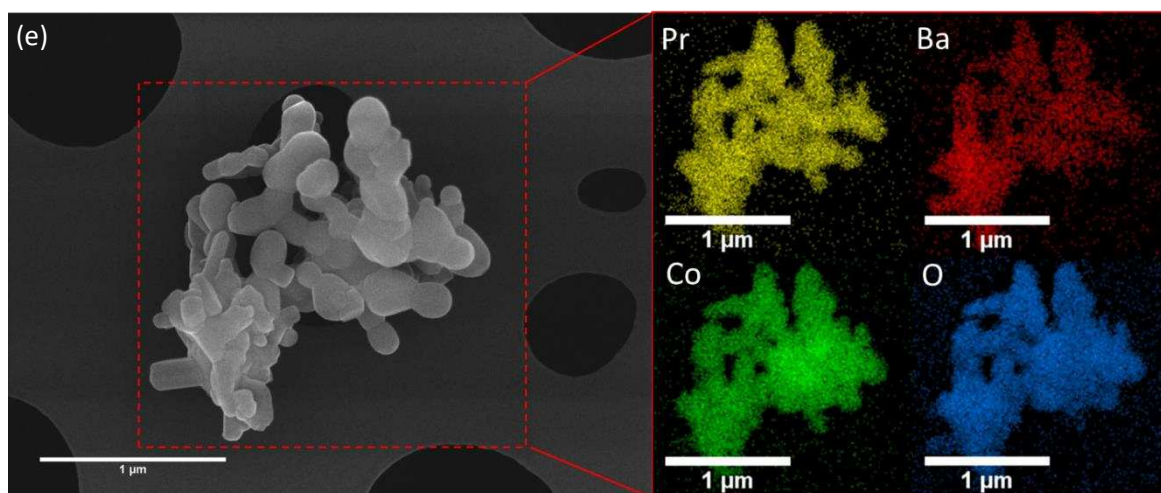
Fig. 1. (a) TGA profile and corresponding derivative as a function of temperature of $Ba_{0.5}Pr_{0.5}CoO_x$ up to 850 °C at 5 °C min^{-1} in air at 50 ml min^{-1}. (b) *In situ* XRD of $Ba_{0.5}Pr_{0.5}CoO_x$ treated to 400 °C prior to analysis heated from 550 °C to 850 °C in air (25 ml min^{-1}). (c) XRD of final calcined BPC perovskite structures. ♦ - $BaPrO_3$ impurity. All other reflections are perovskite phase. (d) Graph showing N_2O decomposition using a BPC perovskite based catalyst. Reaction Conditions: 1 % N_2O/He, total flow 100 ml min^{-1}, GHSV: 60 000 h^{-1}. (e) SEM-EDX mapping of BPC heat-treated to 900 °C. Legend: Yellow: Pr, Red: Ba, Green: Co, Blue: O. All scale bars to 1 µm.

From the *in situ* XRD profile of BPC illustrated in Fig. 1 b, it is possible to see the formation and growth of the principal perovskite phase via the reflection at 34 ° 2θ as the temperature increases from 550 to 850 °C. Some of the reflections present in the 550 °C spectra (impure phase) are still present in the 850 °C spectra. At 850 °C, the purity of the perovskite was low where two perovskite phases can be distinguished. Therefore, a higher calcination temperature of 900 °C was selected, resulting in a purity of 77 %. The two phases ($BaPrCoO_3$ and $BaPrO_3$) can be observed despite the high calcination temperature used, indicating that phase separation has occurred in the catalyst during the heat treatment.

The XRD pattern of the final perovskite (Fig. 1 c) highlights the different phases present, revealing that in this BPC catalyst there is a $BaPrO_3$ impurity that it still present despite calcination at high temperatures. Nitrogen adsorption experiments at -196 °C confirmed that the high calcination temperature resulted in a low surface area of 3 $m^2 g^{-1}$, whereas previous reports indicate that much higher surface areas are required for substantial activity.[10,62–64] Based on its low surface area (Table 2) and low purity this material would not be expected to be a very active catalyst for the decomposition of N_2O. The low surface area (3 $m^2 g^{-1}$) can be attributed to the large particles that formed during the high temperature heat treatment (Fig. 1 e). The high temperature enabled crystal growth to occur, without the formation of fused particles. The structure is uniform throughout, with a good dispersion and no obvious signs of phase separation on a micrometre scale.

When tested for the decomposition of N_2O, the temperature at which 50 % N_2O conversion was achieved (T_{50}) was 527 °C (Fig. 1 d). In contrast, the most active perovskite catalyst reported to our knowledge ($Pr_{0.8}Ba_{0.2}MnO_3$) has a T_{50} of 442 °C.[55] As the relatively low catalytic activity of BPC can be assigned to the poor phase purity and the low specific surface area (3 m^2 g^{-1}), the ratio of the A site metals (Pr and Ba) were altered in an attempt to increase the phase purity and consequently increase activity.

The ratio of the A site metal in BPC was altered from $Ba_{0.5}Pr_{0.5}CoO_x$ to $Pr_{0.75}Ba_{0.25}CoO_x$ to prepare a higher purity perovskite, using a citric acid precipitation method (referred to as PBC Citric). Our previous work showed that by using an A site ratio of 3:1 it was possible to form a perovskite at a lower calcination temperature with a higher phase purity.[65] The same citric acid preparation method was used as previously described. Based on previous experience the material was treated in a chamber oven at 200 °C (1°C min^{-1}, 2 h) and calcined at 500 °C (1 °C min^{-1}, 3 h) before *in situ* XRD was used to determine the final calcination temperature.

The TGA profile of PBC Citric is illustrated in Fig. 2 a, the major mass loss events occur at 170 °C (citric acid decomposition), *ca.* 300 °C (Co Pr, and Ba nitrates decomposition) followed by the final decomposition at 570 °C (Ba nitrate). The final major mass loss event occurred at 570 °C, indicating that the pure phase could form at a lower than expected temperature of 550 °C. *In situ* XRD patterns (Fig. 2 b) were obtained from 550 to 850 °C under flowing air over the PBC Citric precursor. Interestingly, the diffraction patterns suggested that the pure phase perovskite was formed at 550 °C, which is remarkably low, 300 °C lower than the BPC perovskite. The principal ABO_3 reflection at 34 ° 2θ is present after heating to 550 °C. This is consistent with the TGA profile and indicates that a pure phase perovskite has formed. Therefore, 550 °C was selected as the calcination temperature.

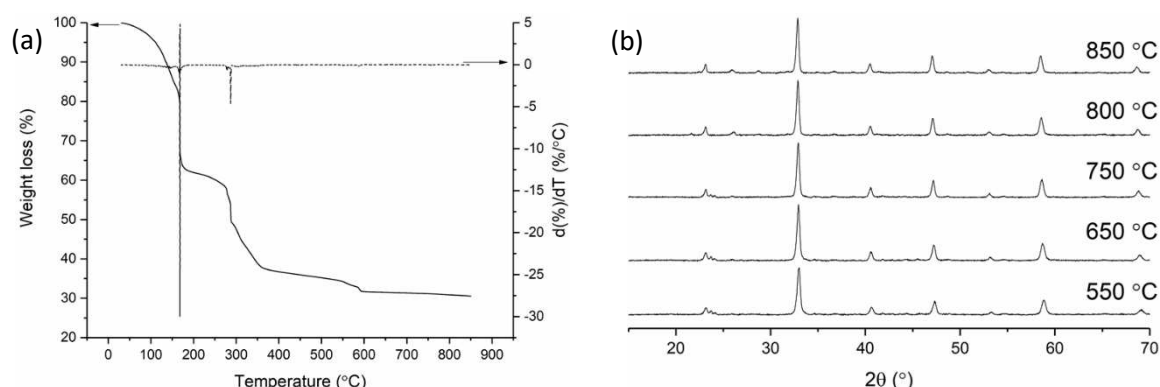Fig. 2. (a) TGA profile and corresponding derivative as a function of temperature of $Pr_{0.75}Ba_{0.25}CoO_x$ up to 850 °C at 5 °C min^{-1} in air at 50 ml min^{-1}. (b) *In situ* XRD of $Pr_{0.75}Ba_{0.25}CoO_x$ treated to 500 °C prior to analysis heated from 550 °C to 850 °C in air (5 ml min^{-1}).

The PBC perovskite catalyst was then prepared by two different preparation methods for comparison, the first was an oxalic acid precipitation method and the second, supercritical anti-solvent preparation, which has been shown previously to produce high surface area perovskites.[34]

The same A site ratio of Pr to Ba was used; however, oxalic acid was selected as the precipitating agent to produce $Pr_{0.75}Ba_{0.25}CoO_x$ (referred to as PBC Oxalic). Oxalic acid facilitates the formation of a network, which then collapse to form a well dispersed metal oxide. As shown previously, TGA was used to determine a suitable pre-treatment temperature as a major mass loss was expected and this would make an untreated sample not suitable for *in situ* XRD. In the case of PBC Oxalic (Fig. 3 a), the last major mass loss occurs *ca.* 600 °C. A significant mass loss below 100 °C was recorded due to the removal of water from the sample, followed by the decomposition of the metal precursors between 250 – 600 °C. Most notably the major mass loss event occurred at 280 °C due to the decomposition of the Co and Pr precursors, with other mass loss events occurring at 175 °C due to oxalic acid decomposition. Between 350 °C and 600 °C, both Ba and Pr nitrate decomposes resulting in major mass loss events over this temperature range. Therefore, 300 °C was selected as a suitable pre-treatment temperature. *In situ* XRD was performed to determine the temperature at which a pure phase perovskite formed. In the case of PBC Oxalic (Fig. 3 b) the perovskite phase does not start to form until 550 °C, with the pure phase forming at 700 °C. The purity of this catalyst reaches a maximum of 96 % at 700 °C; therefore, this temperature was selected for the final calcination temperature. The major reflections are indicative of a tetragonal structure, with the impurities (dotted lines in Fig. 3 b) having a cubic structure. The reflections of the impurity phase were observed at 28.7, 36.6 and 56.5 ° 2θ and are indicative of the presence of PrO_2.

Fig. 3. (a) TGA profile and corresponding derivative as a function of temperature of $Pr_{0.75}Ba_{0.25}CoO_x$ prepared by Oxalic Acid prep up to 850 °C at 5 °C min^{-1} in flowing air at 50 ml min^{-1}. (b) *In situ* XRD of $Pr_{0.75}Ba_{0.25}CoO_x$ treated to 300 °C prior to analysis heated from 550 °C to 850 °C in air (20 ml min^{-1}). Dashed line – Impurities cubic PrO_2. All other reflections tetragonal perovskite phase.

$Pr_{0.75}Ba_{0.25}CoO_x$ was prepared using supercritical anti-solvent precipitation method. This method has been shown previously to produce high surface area perovskites.[34] High surface area perovskites are

characteristically difficult to form; typically a surface area of less than 10 m² g⁻¹ is reported. Given that the active component of a perovskite is at the surface, it follows that higher surface area perovskites are more active, and this is reflected in previous reports.[10,62–64,66,67] Most attempts at increasing the surface area of perovskites have found success through supporting the perovskites on high surface area supports. Alini and co-workers supported a CaMn$_{0.6}$Cu$_{0.4}$O$_3$ perovskite on a CeO$_2$-ZrO$_2$ support and the surface area increased from 15 m² g⁻¹ to 63 m² g⁻¹, with a 10 % perovskite loading. The N$_2$O conversion over the catalyst increased from 58 % to 67 % at 500 °C. The group linked both the increase in surface area and the contribution of the oxygen mobility in the support to the observed increase in activity.[62] However, Dacquin and co-workers reported that it was possible to increase the surface area of LaCoO$_3$ from 12 to 50 m² g⁻¹ by changing the preparation method from templating to reactive grinding. The highest surface area catalysts were correlated with the highest activity for N$_2$O decomposition, with the increase in activity ascribed to the increases in specific surface area and the higher density of oxygen vacancies present.[67]

TGA was once again used to determine a suitable pre-treatment temperature. The TGA of the PBC SAS sample (Fig. 4 a) revealed that all major loss events occurred below 650 °C. The first major mass loss event that occurred below 100 °C and was assigned to the evaporation of ethanol and water from the sample, which are used in the preparation. This was followed by the decomposition of the metal precursors between 150 – 640 °C. There are many mass loss events that occur over the temperature range 150- 640 °C due to the decomposition of the following precursors, Pr acetate (170, 275-380 and 560 °C), Ba acetate (225, 325, 445 and 500 °C) and Co acetate (90, 135, 215 and 315 °C). Therefore, 300 °C was selected as a suitable pre-treatment temperature in the chamber furnace (300 °C at 1 °C min⁻¹ for 2 hours). *In situ* XRD was performed to determine the temperature at which a pure phase perovskite is formed. In the case of the PBC SAS sample (Fig. 4 b), the perovskite phase does not start to form until 600 °C, with a 100 % pure phase forming at 700 °C. The same reflections can be observed in all spectra taken above 700 °C, which is an indication of final phase formation. The reflections are indicative of an orthorhombic structure.

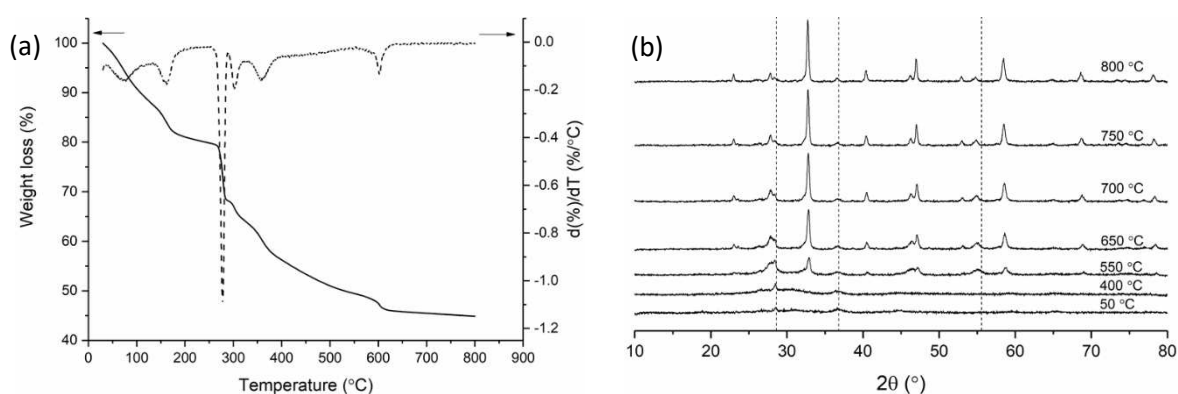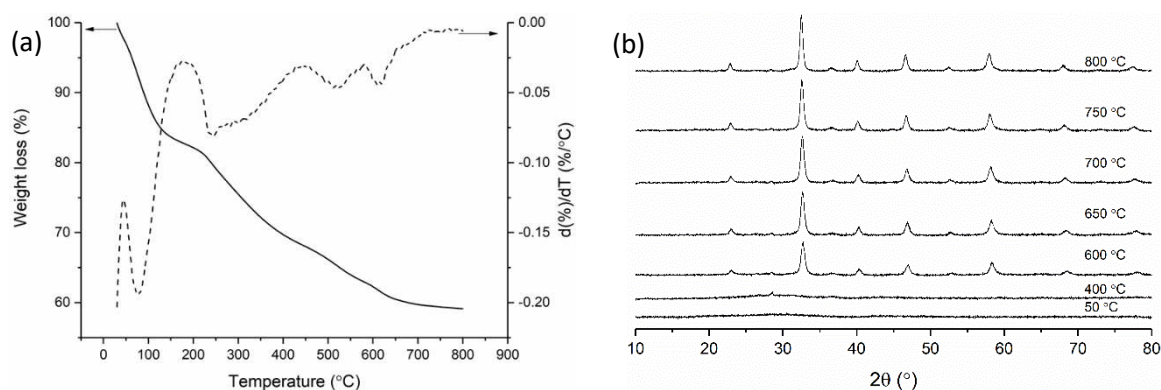Fig. 4. (a) TGA profile and corresponding derivative as a function of temperature of $Pr_{0.75}Ba_{0.25}CoO_x$ prepared by SAS up to 850 °C at 5 °C min^{-1} in flowing air at 50 ml min^{-1}. (b) *In situ* XRD of $Pr_{0.75}Ba_{0.25}CoO_x$ treated to 300 °C prior to analysis heated from 550 °C to 850 °C in air (20 ml min^{-1}).

Illustrated in Fig. 1 d and **Error! Reference source not found.** are the catalytic activities of the BPC and PBC class of catalysts, with N_2O conversion over BPC increasing from 7 % at 450 °C to 58 % over the PBC citric catalyst (T_{50} from 527 °C, to 445 °C). The decomposition rate at 450 °C increased from 3.2 mol h^{-1} kg^{-1} (BPC) to 23.5 mol h^{-1} kg^{-1} (PBC citric) when changing the ratio of the A site metals. The change in catalytic activity between these two catalysts suggests that the increase in phase purity and the increase in surface area (12 m^2 g^{-1} compared to 3 m^2 g^{-1}) has led to a higher activity. We consider the higher surface area is due to the low calcination temperature required to form a pure phase perovskite. Typically, the higher the heat treatment the lower the surface area as the macro-structure can collapse or sinter during the heating process.

In the case of the PBC series, all preparation methods led to the production of catalysts with high activity for N_2O decomposition above 500 °C (**Error! Reference source not found.**). However, at temperatures lower than this the difference in activity is more notable, with the oxalic acid catalyst exhibited a T_{50} of 431 °C and a space time yield at 450 °C of 27.6 mol h^{-1} kg^{-1}, compared to T_{50} of 445 °C for the citric catalyst and T_{50} of 410 °C for the SAS catalyst. The TON and TOF are given in Table S4, however a space time yield is more comparable for these catalysts. The PBC oxalic catalyst contains a 4 % PrO_2 impurity. PrO_2 was tested for N_2O decomposition (Fig. S2) and was shown to have low activity (T_{50} of 593 °C), therefore the impact on the activity of this small impurity was considered negligible. When comparing the surface area normalised reaction data (Table 2), the PBC Oxalic catalyst would be deemed the most active. This is due to the lower surface area (14 m^{2}g^{-1}) and high activity (T_{50} 431 °C). However, the SAS is still deemed active due to the lower T_{50} and high space time yield at 450 °C (32 mol h^{-1} kg^{-1}) achieved by this catalyst.
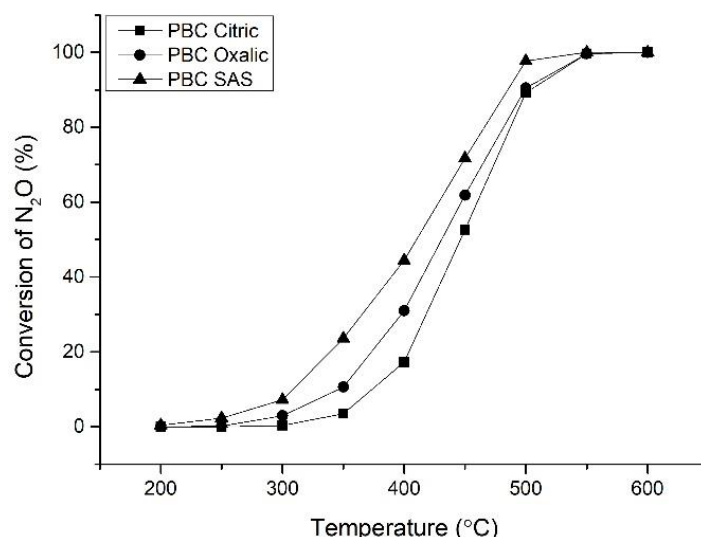
Fig. 5. Effect of preparation method on $Pr_{0.75}Ba_{0.25}CoO_x$ for N_2O decomposition over the temperature range of 200 to 600 °C. Reaction conditions: 1 % N_2O/He, total flow 100 ml min^{-1}.

Analysis of the O 1s region from XPS measurements gives an indication of the species of oxygen present on the surface of the catalyst. There are four notable oxygen species: lattice oxygen O^{2-} from lanthanide at 528.6 eV,[68–71] lattice oxygen species due to transition metal species at *ca.* 529.5 eV (Co or Fe),[72–75] hydroxyl species OH$^-$ at 531 eV,[76] and finally surface adsorbed molecular water at 533 eV.[77–88] The water is trapped within the lattice, rather than being physisorbed on the surface as this would be removed under the ultra-high vacuum conditions required for XPS. Lattice oxygen is also referred to as β-oxygen, with adsorbed O_2^{2-}/O^- species being referred to as α-oxygen or oxygen vacancies.[77,89] The oxygen species present in a perovskite structure have been shown to play a large part in the activity of the N_2O decomposition catalyst.[42–45] Through analysis of the XPS O 1s region of PBC (Fig. 6 a) it should be possible to predict catalytic performance, as the activity is expected to correlate with the lattice oxygen concentration.

The oxygen region of the X-ray photoelectron spectra recorded with BPC (Fig. 6 a) shows the presence of four oxygen species. The surface oxygen present is generally in the form of lattice oxygen from lanthanide elements (20 %), with the remainder comprised of lattice oxygen from transition metals and hydroxyl species. In the case of the citric acid prepared PBC (Fig. 6 a), 19.1 % of the oxygen species present were in the form of lanthanide lattice oxygen (with another 20 % contributed by the transition metal lattice oxygen species); in the oxalic acid PBC catalyst (Fig. 6 a), 26.7 % was lattice oxygen, while PBC SAS (Fig. 6 a) contained 24.5 % lattice oxygen. Therefore, based on the increase in purity and surface area, but similar lattice O^{2-}, all PBC catalysts were predicted to outperform the BPC catalyst.
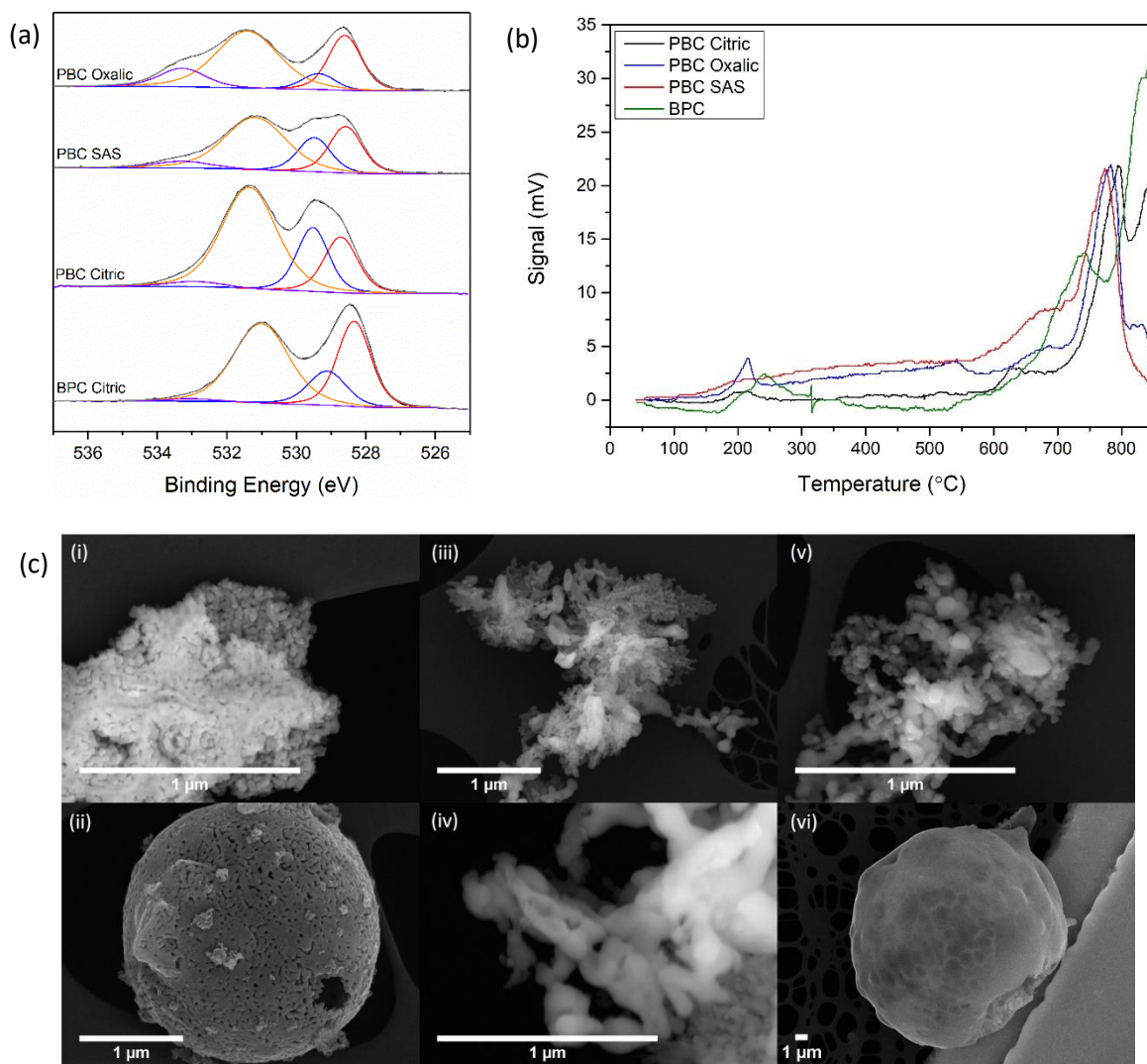
Fig. 6. (a) O 1s region of LSC, BPC and SCF catalysts. Fittings: Red – lattice O^{2-}, Blue – lattice O^{2-} transition metal, Orange – hydroxyl species OH^- and Purple – molecular water on surface. (b) Oxygen temperature programmed desorption (O_2-TPD) of $Pr_{0.75}Ba_{0.25}CoO_x$ and $Ba_{0.5}Pr_{0.5}CoO_x$ catalysts, Black – PBC Citric prep, Red – PBC SAS prep, Blue – PBC Oxalic prep, Green – BPC Citric prep. (c) SEM and SEM-EDX mapping of PBC catalysts, all scale bars 1 μm. Legend: (i and ii) – PBC Citric, (iii and iv) – PBC Oxalic, (v and vi) – PBC SAS.

SEM images of all three PBC perovskites show different morphology depending on preparation method (Fig. 6 c). The PBC citric catalyst shows large hollow microspheres (Fig. 6 c, ii) that account for around 50 % of the morphology, with the other 50 % being a fused morphology (as seen in Fig. 6 c, i). The metals are well dispersed throughout the perovskite structure as shown in the supplementary information (Fig. S3-5). The PBC oxalic catalyst also has two morphologies present: agglomerations of small spheres, intermixed with larger elongated fused particles, both of which can be seen in Fig. 6 c, iii and iv. With two morphologies present there is concern that the dispersion of metals may not be even, however the EDX mapping in Fig. S4 shows that the distribution of the metal components is consistent throughout. Finally, the PBC SAS catalyst shows both large spheres, and a partially fused

structure (Fig. 6 c, v and vi). This is in line with previous work which shows that the preparation of catalysts using the SAS precipitation method had led to the formation of spheres. [34,90–92] The high surface area of this catalyst (Table 2) can be attributed to the formation of initial small particles typically in the scale of nanometres, that are dried under supercritical CO_2, where by the solvent is extracted to retain the pore structure. The formation of carbonate precursor also ensures that the decomposition to a perovskite structure is as gentle as possible with no major precursor decomposition events that would lead to sintering. TEM of PBC SAS shown in Fig. S6. shows that the structure of the catalyst is the same throughout, indicating that there are no amorphous impurities present in the catalyst.

The trend observed in catalytic N_2O decomposition activity (**Error! Reference source not found.**) is not strictly associated with lattice oxygen concentration (Table 2). We consider that lattice oxygen does influence the activity; however, it is not the sole contributing factor, as greater access to the active sites through enhanced surface area can play a role. The activity in terms of lattice oxygen should follow the order, PBC oxalic as the most active > PBC SAS > PBC citric. However, the activity trend observed in this study is: PBC SAS > PBC oxalic > PBC citric.

Table 2. Comparison between all catalysts, preparation method, composition determined by MP-AES, surface area, phase purity and the temperature required for 50 % conversion (T_{50}).

Catalyst	Prep method	Calcination Temperature (°C)	Perovskite Phase Purity (%)[a]	Specific Surface area (m^2 g^{-1})	T_{50} (°C)	Decomposition rate at 450 °C [c] (mol h^{-1} kg^{-1})	Decomposition rate at 450 °C [d] (mol h^{-1} m^{-2})	Lattice O (%)[b]
BPC	Citric Acid	900	77	3	527	3.2	1.05 x10^{-3}	33.0
PBC	Citric Acid	550	100	12	445	23.5	1.96 x10^{-3}	19.1
PBC	SAS	700	100	30	410	32.0	1.07 x10^{-3}	24.5
PBC	Oxalic	700	96	14	431	27.6	1.97 x10^{-3}	26.7

[a] Perovskite phase purity calculated using XRD diffraction pattern and the ratio between the single perovskite phase and any impurities.
[b] Lattice oxygen calculated by the ratio of lattice oxygen species to the sum of molecular water, hydroxyl species, adsorbed O_2^{2-}/O^- as derived from XPS measurements.
[c] N_2O Decomposition rate at 450 °C normalised to weight of catalyst used in reaction.
[d] N_2O Decomposition rate at 450 °C normalised to surface area of catalyst used in reaction.

The surface area of the PBC SAS catalyst is 30 m^2 g^{-1} compared to 14 m^2 g^{-1} for the oxalic acid prepared material and 12 m^2 g^{-1} for the citric acid prepared materials. Therefore, when the N_2O conversion data are normalised to surface area, the oxalic acid prepared PBC catalyst outperforms the other two preparation methods (Table 2). This catalyst has the highest percentage of lattice oxygen, which have a good mobility, as shown by O_2-TPD (Fig. 6 b). This thermal analysis technique provides information about the different oxygen species present in the catalysts. There are normally three species of oxygen

present in the catalysts, all of which desorb at different temperatures. Desorption below 300 °C indicates that chemically adsorbed O_2 is present. α-Oxygen desorbs at 300 – 550 °C, which is oxygen that is removed from the surface to form an oxygen vacancy.[30,89] An oxygen vacancy is formed when oxygen is removed from the surface lattice structure, in the form of O_2 or H_2O, creating a defect site.[93,94] Finally, above 550 °C, bulk lattice oxygen (β-O) desorbs.[30,81,89,95–97] The PBC catalyst series closely follows a trend in which the lattice mobility determines the N_2O decomposition activity. All catalysts show no notable signal response in the region 300 to 550 °C, indicating low surface oxygen vacancies. The SAS catalyst has the earliest onset of a signal response between the region of 550 and 850 °C (Fig. 6 b), that is assigned to the removal of bulk lattice oxygen which will in turn create oxygen vacancies, which present as defect sites on which a reaction can occur as potentially the active site. The lattice oxygen removal originates from the reduction of the B site cation (Co^{3+}/Co^{2+}), generating oxygen vacancies.[98] The introduction of Ba^{2+} ions into the A site ($Pr^{3+/4+}$) also creates oxygen vacancies with in the perovskite $ABCoO_3$ structure.[42]

As shown in Fig. 6 b, the peak ascribed to lattice oxygen for the SAS catalyst is at the lowest temperature (775 °C) and therefore has the lattice oxygen species with the highest mobility (largest signal response between 550 and 700 °C) out of the three preparation methods. The PBC oxalic catalyst has a similar signal response as the PBC SAS catalyst, but the increase in signal between 550 and 700 °C is not as prominent (reduced mobility). However, the sharp desorption peak at 785 °C is at a similar height to the PBC SAS catalyst indicating that there is a similar number of lattice oxygen species released at this temperature although overall lower due to the difference in detector response between 550 and 700 °C. This results in the catalyst displaying the second highest catalytic activity. We consider that the citric acid prepared catalyst has the lowest catalytic activity as it has the least oxygen vacancies out of the three PBC catalysts and the least mobile lattice oxygen (795 °C). The BPC catalyst has no signal response in the region between 300 and 700 °C, indicating that there are no oxygen defects on the surface. Although there is a large signal response at 740 °C due to the desorption of lattice oxygen, the low surface area (3 $m^2\,g^{-1}$) limits the catalytic activity of this catalyst. Oxygen mobility can be studied by a combination of O_2-TPD and H_2-TPR, the earlier onset of the lattice oxygen desorption and the lower the temperature at which the B site metal reduction takes place at indicate a higher oxygen mobility.[99] A low oxygen mobility may limit oxygen recombination after N_2O has adsorbed and dissociated to N_2 and O on the surface.[100–106] As the adsorbed O must combine with another O species to form O_2, if the surface species are not mobile then this step becomes rate determining. Therefore, the most active catalyst can be considered to possess the most oxygen defects formed by removal of lattice oxygen species and the most mobile lattice oxygen.

The H_2-TPR profile represents the reducibility of the perovskites, which is associated with its ability to liberate oxygen from the catalyst by reaction with H_2. H_2-TPR also gives an indication to the strength of the Co-O bond, the weaker this bond the more mobile the oxygen species.[107] The reduction of surface adsorbed O species or excess oxygen species take place between 200 and 300 °C.[108] This is followed by the step wise reduction of Co^{3+} to Co^{2+} between 200 and 360 °C, and Co^{2+} to Co^0 between 450 and 540 °C.[109–111] Pr^{4+} and Ba^{2+} species are not reducible in the temperature range studied.[98,112] In the BPC catalyst (Fig. S9) there is a peak between 250 and 360 °C assigned to the reduction of Co^{3+} to Co^{2+}. The peak also has a shoulder in the range 150 − 250 °C assigned to the reduction of surface oxygen species. The reduction of Co^{2+} to Co^0 is continuous from Co^{3+} in BPC and take place between 360 and 460 °C. This shift in temperature is due to the presence of Ba and Pr species that have been shown to lower the temperature required to reduce the B site metal in a perovskite structure.[55,98] PBC Citric shows a shoulder between 150 and 250 °C assigned to the reduction of surface oxygen species, followed by the reduction of Co^{3+} to Co^{2+} between 250 and 450 °C, then followed by the reduction of Co^{2+} to Co^0 between 450 and 560 °C. PBC Oxalic shows significant reduction of oxygen species between 200 and 320 °C, followed by the reduction of Co^{3+} to Co^{2+} between 320 and 440 °C, and then the subsequent reduction of Co^{2+} to Co^0 between 440 and 550 °C. The H_2-TPR of PBC SAS shows initial reduction of surface oxygen species as a shoulder between 100 and 230 °C followed by the reduction of Co^{3+} to Co^{2+} between 230 and 295 °C. The reduction of Co^{2+} to Co^0 take place at a significantly lower temperature in PBC SAS, between 300 and 400 °C, this is due to the electronic effects of both Ba and Pr species.[55,98] Therefore, PBC SAS is the most reducible catalyst, as the reduction steps take place at the lowest temperature, this indicates that the catalyst with the highest oxygen mobility.

The Co 2p region overlaps directly with the Ba 3d region, when coupled with the changing background observed in this case makes it very difficult to model. Therefore, shown in Fig. S10. is the Co 3p spectra which does not overlap with any other components of the material. Deconvolution of the spectra is challenging due to its subjective nature, instead, we are looking simply at the line shapes present. The BPC catalyst contains the most Ba, it is therefore expected that this catalyst would have the highest ratio of Co^{2+}/Co^{3+}, which would result in a marginally broader line shape, as reported in literature. [78,81,108,113–115] As shown by H_2-TPR (Fig. S9), PBC SAS was found to be the most reducible, and therefore has the highest redox properties. We consider that these redox properties would lead to a higher Co^{2+}/Co^{3+} ratio, and a broader line shape, which is seen. The PBC Oxalic and PBC Citric catalysts show the same line shape, indicating that they have very similar ratios of Co^{2+}/Co^{3+} and therefore redox properties, which supports our analysis of the H_2-TPR data.

All three PBC perovskite have different unit cell structures, (PBC Citric Cubic, PBC oxalic tetragonal and PBC SAS orthorhombic) therefore it is not possible to compare the unit cell parameters in Table S3,

without first calculating the pseudo cubic unit cell.[116] Cordier shows that all structures are very similar, with the difference being related to the octahedra of the A site, with the octahedra being tilted and the atoms displaced from the centre of the octahedral sites. [116] Therefore, it is possible to calculate a pseudo cubic unit cell for these structures, leading to the calculation of a pseudo cubic cell volume. All three non-cubic structured materials have an increased pseudo cell volume, this is due to an increase in the distortion of the material, based on the changes to the A site octahedra. PBC oxalic has the largest pseudo cubic cell volume, 57.8×10^{6} pm^3, with PBC SAS having the second largest at 55.3×10^{6} pm^3. The higher pseudo cubic cell volume of PBC oxalic would indicate that the catalyst would be the most distorted and therefore have the greatest number of defects and potentially oxygen vacancies, but this is not shown in the O_2-TPD. PBC SAS has a slightly smaller pseudo cubic cell volume than the oxalic catalyst, again indicating an increase in distortion and defects. This coupled with the high surface area of 30 m^2 g^{-1} leads to a highly active catalyst.

The most active PBC SAS catalyst was tested for 22 hours to show stability, (Fig. S8) this showed that the catalyst was extremely stable, with the activity remaining at 51 % conversion over the time period tested, showing no deactivation.

Table 2 compares all catalysts discussed in the current work. When noting the trends it is possible to see that by changing the ratio from BPC (where Ba and Pr are 1:1 in the A site) to PBC (where Pr:Ba is 3:1 in the A site), the purity increases from 77 % to 100 %, while the T_{50} decreases from 527 to 445 °C (using the same preparation method). Therefore, changing the ratio improved the purity and surface area and subsequently the catalytic activity. When comparing the three preparation methods for the PBC catalyst, the SAS prepared catalyst has the lowest T_{50} (410 °C), and highest decomposition rate. There are several factors that can contribute to the differences in activity between preparation methods, namely: (i) the higher surface area that is achieved using the SAS preparation method, (ii) the lattice oxygen mobility, and (iii) the presence of oxygen vacancies within the catalyst.

N_2O decomposition is thought to proceed via the following route: The terminal oxygen of N_2O binds at an oxygen vacancy on the surface of the perovskite. This leads to the destruction of the nitrogen oxygen bond in N_2O resulting in N_2 being emitted and oxygen remaining on the surface. These newly bound oxygen species are mobile and therefore can travel across the surface to recombine with other deposited oxygen species resulting in regeneration of the active site.

Overall, the SAS preparation method produces the catalyst with the most reducible Co species and has the earliest onset of signal in the β-O region. This suggests that PBC SAS has the most mobile lattice oxygen species and the most oxygen vacancies available over a relatively high surface area of 30 m^{2}g^{-1}, when considering the mechanism, it is easy to see why this is the most active catalysts in the series.

Conclusions

The current work has demonstrated that high surface area, high purity perovskites can be prepared by using supercritical anti-solvent precipitation. Careful control of the composition of the A site, and the preparation method used, enabled formation of high surface area perovskite phases at relatively low temperature, which minimised thermal agglomeration and collapse of the macro-structure.

This work has also confirmed the importance of lattice oxygen species that have high oxygen mobility for the decomposition of N_2O. Mobile lattice oxygen has been shown to be crucial, as the rate-limiting step in the decomposition of N_2O is the formation of oxygen from molecular oxygen that is deposited on the active site of the catalyst.[57,100–106] Our data illustrates that a higher density of oxygen vacancies led to a more active catalyst, by providing a greater number of active sites. The most active catalyst with respect to a T_{50} value was prepared via the SAS method, as this catalyst had a combination of both the largest amount of mobile lattice oxygen and the highest surface area over which the active sites are distributed. The high phase purity, high oxygen mobility and high surface area of the PBC SAS catalyst suggest that this material could be applied to a number of systems, such as photovoltaic systems, including solar cells in addition to suitable catalytic reactions.[35–40] When compared to relevant literature examples (Table 1), the PBC SAS outperform that of Kumar *et al.* with a T_{50} of 442 °C and a decomposition rate of 1.2 mol h^{-1} kg^{-1} using a $Pr_{0.2}Ba_{0.8}MnO_3$ catalyst,[55] whereas the PBC SAS catalyst tested here have a T_{50} of 410 °C and a decomposition rate of 32 mol h^{-1} kg^{-1} at 450 °C.

Table of Contents/Graphical Abstract
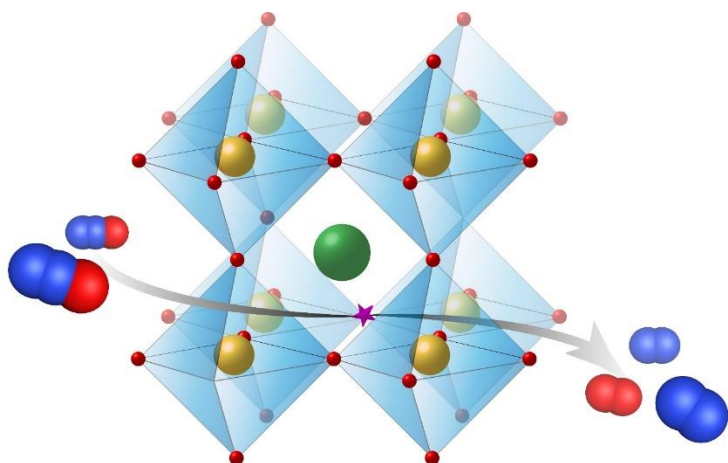
Supporting Information

TGA of catalyst precursors, N_2O decomposition activity of PrO_2 impurity, SEM-EDX of PBC catalysts, TEM of PBC Citric, catalytic activity data as a function of time and temperature for all catalysts, time on line data for PBC SAS, TPR of all catalysts, Co 3p XPS spectra and the unit cell parameters used in the manuscript are supplied as Supporting Information. This material is available free of charge via the Internet   at

https://eur03.safelinks.protection.outlook.com/?url=http%3A%2F%2Fpubs.acs.org%2F&data=0 2%7C01%7CRichardsN8%40cardiff.ac.uk%7C22887f281df140535fa608d7e089495b%7Cbdb74b3095 684856bdbf06759778fcbc%7C1%7C0%7C637224752553592168&sdata=8pafJja%2B6jLSnmBPN 63gFP4CX7seezgtUgQ3ZCTVtUs%3D&reserved=0.

References

(1)   Pérez-Ramírez, J.; Kapteijn, F.; Schöffel, K.; Moulijn, J. A. Formation and Control of N2O in Nitric Acid Production: Where Do We Stand Today? *Appl. Catal. B Environ.* **2003**, *44*, 117–151.

(2)   Weimann, J. Toxicity of Nitrous Oxide. *Best Pract. Res. Clin. Anaesthesiol.* **2003**, *17*, 47–61.

(3)   Grace, P.; Barton, L. http://theconversation.com/meet-n2o-the-greenhouse-gas-300-times-worse-than-co2-35204.

(4)   Intergovernmental Panel on Climate Change. *Climate Change 2007 Synthesis Report*; 2008.

(5)   Li, L.; Xu, J.; Hu, J.; Han, J. Reducing Nitrous Oxide Emissions to Mitigate Climate Change and Protect the Ozone Layer. *Environ. Sci. Technol.* **2014**, *48*, 5290–5297.

(6)   Intergovernmental Panel on Climate Change. *Climate Change 2013: The Physical Science Basis. Contribution of Working Group I to the Fifth Assessment Report of the Intergovernmental Panel on Climate Change*; 2013.

(7)   Jabłońska, M.; Palkovits, R. It Is No Laughing Matter: Nitrous Oxide Formation in Diesel Engines and Advances in Its Abatement over Rhodium-Based Catalysts. *Catal. Sci. Technol.* **2016**, *6*, 7671–7687.

(8)   UNEP. *Drawing Down Nitrous Oxide To Protect Climate and the Ozone Layer*; 2013.

(9)   Maroufi, S. S.; Gharavi, M. J.; Behnam, M.; Samadikuchaksaraei, A. Nitrous Oxide Levels in Operating and Recovery Rooms of Iranian Hospitals. *Iran. J. Public Health* **2011**, *40*, 75–79.

(10)   Kapteijn, F.; Rodriguez-Mirasol, J.; Moulijn, J. A. Heterogeneous Catalytic Decomposition of Nitrous Oxide. *Appl. Catal. B Environ.* **1996**, *9*, 25–64.

(11)   Zabilskiy, M.; Erjavec, B.; Djinović, P.; Pintar, A. Ordered Mesoporous CuO-CeO2 Mixed Oxides as an Effective Catalyst for N2O Decomposition. *Chem. Eng. J.* **2014**, *254*, 153–162.

(12)   Zhou, H.; Hu, P.; Huang, Z.; Qin, F.; Shen, W.; Xu, H. Preparation of NiCe Mixed Oxides for Catalytic Decomposition of N2O. *Ind. Eng. Chem. Res.* **2013**, *52*, 4504–4509.

(13)   Zhou, H.; Huang, Z.; Sun, C.; Qin, F.; Xiong, D.; Shen, W.; Xu, H. Catalytic Decomposition of N2O over CuxCe1-XOymixed Oxides. *Appl. Catal. B Environ.* **2012**, *125*, 492–498.

(14)   Abu-Zied, B. M.; Soliman, S. A.; Abdellah, S. E. Enhanced Direct N2O Decomposition over CuXCo1-XCo2O4(0.0≤x≤1.0) Spinel-Oxide Catalysts. *J. Ind. Eng. Chem.* **2015**, *21*, 814–821.

(15)   Stelmachowski, P.; Maniak, G.; Kaczmarczyk, J.; Zasada, F.; Piskorz, W.; Kotarba, A.; Sojka, Z.

Mg and Al Substituted Cobalt Spinels as Catalysts for Low Temperature DeN2O-Evidence for Octahedral Cobalt Active Sites. *Appl. Catal. B Environ.* **2014**, *146*, 105–111.

(16)   Amrousse, R.; Tsutsumi, A.; Bachar, A.; Lahcene, D. N2O Catalytic Decomposition over Nano-Sized Particles of Co-Substituted Fe3O4 Substrates. *Appl. Catal. A Gen.* **2013**, *450*, 253–260.

(17)   Parres-Esclapez, S.; Illan-Gomez, M. J.; de Lecea, C. S. M.; Bueno-Lopez, A. On the Importance of the Catalyst Redox Properties in the N2O Decomposition over Alumina and Ceria Supported Rh, Pd and Pt. *Appl. Catal. B Environ.* **2010**, *96*, 370–378.

(18)   Yuzaki, K.; Yarimizu, T.; Ito, S.; Kunimori, K. Catalytic Decomposition of N2O over Supported Rhodium Catalysts: High Activities of Rh/USY and Rh/Al2O3 and the Effect of Rh Precursors. *Catal. Letters* **1997**, *47*, 173–175.

(19)   Kapteijn, F.; Mul, G.; Marbán, G.; Rodriguez-Mirasol, J.; Moulijn, J. A. Decomposition of Nitrous Oxide over ZSM-5 Catalysts. In *11th International Congress on Catalysis - 40th Anniversary, Volume 101*; 1996; Vol. 101, pp 641–650.

(20)   Kordulis, C.; Latsios, H.; Lycourghiotis, A.; Pomonis, P. Kinetics of N2o Decomposition on Fe-3+ Supported on Pure and Li-Modified Al2o3. *Int. J. Chem. Tech. Res.* **2015**, *88*, 201–205.

(21)   Li, Y.; Armor, J. N. Catalytic Decomposition of Nitrous Oxide on Metal Exchanged Zeolites. *Appl. Catal. B, Environ.* **1992**, *1*, 1–9.

(22)   Konsolakis, M. I. Recent Advances on Nitrous Oxide (N2O) Decomposition over Non–Noble Metal Oxide Catalysts: Catalytic Performance, Mechanistic Considerations and Surface Chemistry Aspects. *ACS Catal.* **2015**, *5*, 6397–6421.

(23)   Hwang, J.; Rao, R. R.; Giordano, L.; Katayama, Y.; Yu, Y.; Shao-Horn, Y. Perovskites in Catalysis and Electrocatalysis. *Science (80-.).* **2017**, *358*, 751–756.

(24)   Voorhoeve, R. J. H.; Johnson, D. W.; Remeika, J. P.; Gallagher, P. K. Perovskite Oxides : Materials Science in Catalaysis. *Science (80-.).* **1977**, *195*, 827–833.

(25)   Peña, M. A.; Fierro, J. L. G. Chemical Structures and Performance of Perovskite Oxides. *Chem. Rev.* **2001**, *101*, 1981–2017.

(26)   Centi, G.; Perathoner, S. Catalysis by Layered Materials: A Review. *Microporous Mesoporous Mater.* **2008**, *107*, 3–15.

(27)   Isupova, L. A.; Alikina, G. M.; Tsybulya, S. V; Boldyreva, N. N.; Kryukova, G. N.; Yakovleva, I. S.; Isupov, V. P.; Sadykov, V. A. Real Structure and Catalytic Activity of La1–xSrxCoO3 Perovskites.

Int. J. Inorg. Mater. **2001**, *3*, 559–562.

(28)   Zhu, J.; Xiao, D.; Li, J.; Xie, X.; Yang, X.; Wu, Y. Recycle - New Possible Mechanism of NO Decomposition over Perovskite(-like) Oxides. *J. Mol. Catal. A Chem.* **2005**, *233*, 29–34.

(29)   Zhu, J.; Yang, X.; Xu, X.; Wei, K. Active Site Structure of NO Decomposition on Perovskite(-like) Oxides: An Investigation from Experiment and Density Functional Theory. *J. Phys. Chem. C* **2007**, *111*, 1487–1490.

(30)   Zhu, J.; Zhao, Z.; Xiao, D.; Li, J.; Yang, X.; Wu, Y. Study of La2-XSrxCuO4 (x = 0.0, 0.5, 1.0) Catalysts for NO + CO Reaction from the Measurements of O2-TPD, H2-TPR and Cyclic Voltammetry. *J. Mol. Catal. A Chem.* **2005**, *238*, 35–40.

(31)   Huang, C.; Wang, X.; Shi, Q.; Liu, X.; Zhang, Y.; Huang, F.; Zhang, T. A Facile Peroxo-Precursor Synthesis Method and Structure Evolution of Large Specific Surface Area Mesoporous BaSnO 3. *Inorg. Chem.* **2015**, *54*, 4002–4010.

(32)   Huang, F.; Wang, X.; Wang, A.; Xu, J.; Zhang, T. A Two-Step Synthesis of Fe-Substituted Hexaaluminates with Enhanced Surface Area and Activity in Methane Catalytic Combustion. *Catal. Sci. Technol.* **2016**, *6*, 4962–4969.

(33)   Afzal, S.; Quan, X.; Zhang, J. High Surface Area Mesoporous Nanocast LaMO3 (M = Mn, Fe) Perovskites for Efficient Catalytic Ozonation and an Insight into Probable Catalytic Mechanism. *Appl. Catal. B Environ.* **2017**, *206*, 692–703.

(34)   Evans, C. D.; Kondrat, S. A.; Smith, P. J.; Manning, T. D.; Miedziak, P. J.; Brett, G. L.; Armstrong, R. D.; Bartley, J. K.; Taylor, S. H.; Rosseinsky, M. J.; Hutchings, G. J. The Preparation of Large Surface Area Lanthanum Based Perovskite Supports for AuPt Nanoparticles: Tuning the Glycerol Oxidation Reaction Pathway by Switching the Perovskite B Site. *Faraday Discuss.* **2016**, *188*, 427–450.

(35)   Meng, L.; Sun, C.; Wang, R.; Huang, W.; Zhao, Z.; Sun, P.; Huang, T.; Xue, J.; Lee, J. W.; Zhu, C.; Huang, Y.; Li, Y.; Yang, Y. Tailored Phase Conversion under Conjugated Polymer Enables Thermally Stable Perovskite Solar Cells with Efficiency Exceeding 21%. *J. Am. Chem. Soc.* **2018**, *140*, 17255–17262.

(36)   Zhang, M.; Dai, S.; Chandrabose, S.; Chen, K.; Liu, K.; Qin, M.; Lu, X.; Hodgkiss, J. M.; Zhou, H.; Zhan, X. High-Performance Fused Ring Electron Acceptor-Perovskite Hybrid. *J. Am. Chem. Soc.* **2018**, *140*, 14938–14944.

(37)   Lee, J. W.; Dai, Z.; Lee, C.; Lee, H. M.; Han, T. H.; De Marco, N.; Lin, O.; Choi, C. S.; Dunn, B.; Koh,

J.; Di Carlo, D.; Ko, J. H.; Maynard, H. D.; Yang, Y. Tuning Molecular Interactions for Highly Reproducible and Efficient Formamidinium Perovskite Solar Cells via Adduct Approach. *J. Am. Chem. Soc.* **2018**, *140*, 6317–6324.

(38) Ahn, N.; Son, D. Y.; Jang, I. H.; Kang, S. M.; Choi, M.; Park, N. G. Highly Reproducible Perovskite Solar Cells with Average Efficiency of 18.3% and Best Efficiency of 19.7% Fabricated via Lewis Base Adduct of Lead(II) Iodide. *J. Am. Chem. Soc.* **2015**, *137*, 8696–8699.

(39) Liu, C.; Li, W.; Zhang, C.; Ma, Y.; Fan, J.; Mai, Y. All-Inorganic CsPbI2Br Perovskite Solar Cells with High Efficiency Exceeding 13%. *J. Am. Chem. Soc.* **2018**, *140*, 3825–3828.

(40) Yang, Z.; Wei, M.; Voznyy, O.; Todorovic, P.; Liu, M.; Quintero-Bermudez, R.; Chen, P.; Fan, J. Z.; Proppe, A. H.; Quan, L. N.; Walters, G.; Tan, H.; Chang, J. W.; Jeng, U. S.; Kelley, S. O.; Sargent, E. H. Anchored Ligands Facilitate Efficient B-Site Doping in Metal Halide Perovskites. *J. Am. Chem. Soc.* **2019**, *141*, 8296–8305.

(41) Ke, W.; Spanopoulos, I.; Tu, Q.; Hadar, I.; Li, X.; Shekhawat, G. S.; Dravid, V. P.; Kanatzidis, M. G. Ethylenediammonium-Based "Hollow" Pb/Sn Perovskites with Ideal Band Gap Yield Solar Cells with Higher Efficiency and Stability. *J. Am. Chem. Soc.* **2019**, *141*, 8627–8637.

(42) Tanaka, H.; Misono, M. Advances in Designing Perovskite Catalysts. *Curr. Opin. Solid State Mater. Sci.* **2001**, *5*, 381–387.

(43) Marchetti, L.; Forni, L. Catalytic Combustion of Methane over Perovskites. *Appl. Catal. B Environ.* **1998**, *15*, 179–187.

(44) Voorhoeve, R. J. H.; Remeika, J. P.; Trimble, L. E. Defect Chemistry and Catalysis in Oxidation and Reduction Over Perovskite-Type Oxides. *Ann. N. Y. Acad. Sci.* **1976**, *272*, 3–21.

(45) Jung, J. Il; Jeong, H. Y.; Lee, J. S.; Kim, M. G.; Cho, J. A Bifunctional Perovskite Catalyst for Oxygen Reduction and Evolution. *Angew. Chemie - Int. Ed.* **2014**, *53*, 4582–4586.

(46) Zhu, J.; Li, H.; Zhong, L.; Xiao, P.; Xu, X.; Yang, X.; Zhao, Z.; Li, J. Perovskite Oxides: Preparation, Characterizations, and Applications in Heterogeneous Catalysis. *ACS Catal.* **2014**, *4*, 2917–2940.

(47) Miedziak, P. J.; Tang, Z.; Davies, T. E.; Enache, D. I.; Bartley, J. K.; Carley, A. F.; Herzing, A. a.; Taylor, S. H.; Hutchings, G. J. Ceria Prepared Using Supercritical Antisolvent Precipitation: A Green Support for Gold-Palladium Nanoparticles for the Selective Catalytic Oxidation of Alcohols. **2009**, *19*, 8619–8627.

(48) Smith, P. J.; Kondrat, S. A.; Carter, J. H.; Chater, P. A.; Bartley, J. K.; Taylor, S. H.; Spencer, M. S.;

Hutchings, G. J. Supercritical Antisolvent Precipitation of Amorphous Copper–Zinc Georgeite and Acetate Precursors for the Preparation of Ambient-Pressure Water-Gas-Shift Copper/Zinc Oxide Catalysts. *ChemCatChem* **2017**, *9*, 1621–1631.

(49) De Jong, K. P. *Synthesis of Solid Catalysts*, 1st ed.; Wiley-VCH Verlag GmbH & Co. KGaA, 2009; Vol. 39.

(50) Trikalitis, P. N.; Pomonis, P. J. Catalytic Activity and Selectivity of Perovskites La1−xSrxV1−x3+Vx4+O3 for the Transformation of Isopropanol. *Appl. Catal. A Gen.* **1995**, *131*, 309–322.

(51) Ishikawa, S.; Jones, D. R.; Iqbal, S.; Reece, C.; Morgan, D. J.; Willock, D. J.; Miedziak, P. J.; Bartley, J. K.; Edwards, J. K.; Murayama, T.; Ueda, W.; Hutchings, G. J. Identification of the Catalytically Active Component of Cu-Zr-O Catalyst for the Hydrogenation of Levulinic Acid to γ-Valerolactone. *Green Chem.* **2017**, *19*, 225–236.

(52) Yuan, J.; Li, S. S.; Yu, L.; Liu, Y. M.; Cao, Y.; He, H. Y.; Fan, K. N. Copper-Based Catalysts for the Efficient Conversion of Carbohydrate Biomass into γ-Valerolactone in the Absence of Externally Added Hydrogen. *Energy Environ. Sci.* **2013**, *6*, 3308–3313.

(53) Wang, L.-C.; Liu, Q.; Chen, M.; Liu, Y.-M.; Cao, Y.; He; Fan, K.-N. Structural Evolution and Catalytic Properties of Nanostructured Cu/ZrO₂ Catalysts Prepared by Oxalate Gel-Coprecipitation Technique. *J. Phys. Chem. C* **2007**, *111*, 16549–16557.

(54) Russo, N.; Mescia, D.; Fino, D.; Saracco, G.; Specchia, V. N2O Decomposition over Perovskite Catalysts. *Ind. Eng. Chem. Res.* **2007**, *46*, 4226–4231.

(55) Kumar, S.; Vinu, A.; Subrt, J.; Bakardjieva, S.; Rayalu, S.; Teraoka, Y.; Labhsetwar, N. Catalytic N2O Decomposition on Pr0.8Ba 0.2MnO3 Type Perovskite Catalyst for Industrial Emission Control. *Catal. Today* **2012**, *198*, 125–132.

(56) Ishihara, T.; Ando, M.; Sada, K.; Takiishi, K.; Yamada, K.; Nishiguchi, H.; Takita, Y. Direct Decomposition of NO into N2 and O2 over La(Ba)Mn(In)O3 Perovskite Oxide. *J. Catal.* **2003**, *220*, 104–114.

(57) Ivanov, D. V.; Sadovskaya, E. M.; Pinaeva, L. G.; Isupova, L. A. Influence of Oxygen Mobility on Catalytic Activity of La-Sr-Mn-O Composites in the Reaction of High Temperature N2O Decomposition. *J. Catal.* **2009**, *267*, 5–13.

(58) Ivanov, D. V.; Pinaeva, L. G.; Isupova, L. A.; Nadeev, A. N.; Prosvirin, I. P.; Dovlitova, L. S. Insights into the Reactivity of La1-XSrxMnO3(x = 0 ÷ 0.7) in High Temperature N2O Decomposition.

Catal. Letters **2011**, *141*, 322–331.

(59) Ivanov, D. V.; Pinaeva, L. G.; Isupova, L. A.; Sadovskaya, E. M.; Prosvirin, I. P.; Gerasimov, E. Y.; Yakovleva, I. S. Effect of Surface Decoration with LaSrFeO4on Oxygen Mobility and Catalytic Activity of La0.4Sr0.6FeO3-Δin High-Temperature N2O Decomposition, Methane Combustion and Ammonia Oxidation. *Appl. Catal. A Gen.* **2013**, *457*, 42–51.

(60) Hutchings, G. J.; Bartley, J. K.; Lopez-Sanchez, J. A.; Carley, A. F.; Rhodes, C.; Webster, J. M.; Gilbert, D. J.; Howdle, S. M.; Poliakoff, M.; Kiely, C. J.; Sajip, S.; Caldarelli, S.; Volta, J. C. Amorphous Vanadium Phosphate Catalysts from Supercritical Antisolvent Precipitation. *J. Catal.* **2001**, *197*, 232–235.

(61) Marin, R. P.; Kondrat, S. A.; Pinnell, R. K.; Davies, T. E.; Golunski, S.; Bartley, J. K.; Hutchings, G. J.; Taylor, S. H. Green Preparation of Transition Metal Oxide Catalysts Using Supercritical CO2 Anti-Solvent Precipitation for the Total Oxidation of Propane. *Appl. Catal. B Environ.* **2013**, *140–141*, 671–679.

(62) Alini, S.; Basile, F.; Blasioli, S.; Rinaldi, C.; Vaccari, A. Development of New Catalysts for N2O-Decomposition from Adipic Acid Plant. *Appl. Catal. B Environ.* **2007**, *70*, 323–329.

(63) Labhasetwar, N.; Saravanan, G.; Kumar Megarajan, S.; Manwar, N.; Khobragade, R.; Doggali, P.; Grasset, F. Perovskite-Type Catalytic Materials for Environmental Applications. *Sci. Technol. Adv. Mater.* **2015**, *16*, 036002.

(64) Russo, N.; Mescia, D.; Fino, D.; Saracco, G.; Specchia, V. N2O Decomposition over Perovskite Catalysts. *Ind. Eng. Chem. Res.* **2007**, *46*, 4226–4231.

(65) Richards, N. The Catalytic Decomposition of Nitrous Oxide, Cardiff University, 2019.

(66) Royer, S.; Duprez, D.; Can, F.; Courtois, X.; Batiot-Dupeyrat, C.; Laassiri, S.; Alamdari, H. Perovskites as Substitutes of Noble Metals for Heterogeneous Catalysis: Dream or Reality. *Chem. Rev.* **2014**, *114*, 10292–10368.

(67) Dacquin, J. P.; Dujardin, C.; Granger, P. Catalytic Decomposition of N2O on Supported Pd Catalysts: Support and Thermal Ageing Effects on the Catalytic Performances. *Catal. Today* **2008**, *137*, 390–396.

(68) Thermofisher.   XPS   Simplified   -   Praseodymium https://xpssimplified.com/elements/praseodymium.php (accessed Mar 19, 2019).

(69) Thermofisher. XPS Simplified - Barium https://xpssimplified.com/elements/barium.php

(accessed Mar 19, 2019).

(70)   Thermofisher. XPS Simplified - Strontium https://xpssimplified.com/elements/strontium.php (accessed Mar 19, 2019).

(71)   Thermofisher. XPS Simplified - Lanthanum https://xpssimplified.com/elements/lanthanum.php (accessed Mar 19, 2019).

(72)   Fierro, J. L. G.; Tejuca, L. G. Non-Stoichiometric Surface Behaviour of LaMO3 Oxides as Evidenced by XPS. *Appl. Surf. Sci.* **1987**, *27*, 453–457.

(73)   Tabata, K.; Hirano, Y.; Suzuki, E. XPS Studies on the Oxygen Species of LaMn1-XCuxO3+λ. *Appl. Catal. A Gen.* **1998**, *170*, 245–254.

(74)   Thermofisher. XPS Simplified - Iron https://xpssimplified.com/elements/iron.php (accessed Mar 19, 2019).

(75)   Thermofisher. XPS Simplified - Cobalt https://xpssimplified.com/elements/cobalt.php (accessed Mar 19, 2019).

(76)   Morris, M. A.; Connell, M. O.; Norman, A. K.; Hu, C. F. Catalytic Oxidation over Lanthanum-Transition Metal Perovskite Materials. *Catal. Today* **1999**, *47*, 123–132.

(77)   Worayingyong, A.; Kangvansura, P.; Kityakarn, S. Schiff Base Complex Sol-Gel Method for LaCoO3perovskite Preparation with High-Adsorbed Oxygen. *Colloids Surfaces A Physicochem. Eng. Asp.* **2008**, *320*, 123–129.

(78)   Zhang-Steenwinkel, Y.; Beckers, J.; Bliek, A. Surface Properties and Catalytic Performance in CO Oxidation of Cerium Substituted Lanthanum-Manganese Oxides. *Appl. Catal. A Gen.* **2002**, *235*, 79–92.

(79)   Wang, P.; Yao, L.; Wang, M.; Wu, W. XPS and Voltammetric Studies on La Sr CoO Perovskite Oxide Electrodes. *J. Alloys Compd.* **2000**, *311*, 53–56.

(80)   Sui, C.; Niu, X.; Wang, Z.; Yuan, F.; Zhu, Y. Activity and Deactivation of Ru Supported on La1.6Sr0.4NiO4 Perovskite-like Catalysts Prepared by Different Methods for Decomposition of N2O. *Catal. Sci. Technol.* **2016**, *6*, 8505–8515.

(81)   Kumar, S.; Teraoka, Y.; Joshi, A. G.; Rayalu, S.; Labhsetwar, N. Ag Promoted La0.8Ba0.2MnO3 Type Perovskite Catalyst for N2O Decomposition in the Presence of O2, NO and H2O. *J. Mol. Catal. A Chem.* **2011**, *348*, 42–54.

(82)   Bianconi, A.; Kotani, A.; Okada, K.; Giorgi, R.; Gargano, A.; Marcelli, A.; Miyahara, T. Many-Body Effects in Praesodyminm Core-Level Spectroscopies of Pr02 Dipartimento. *Am. Phys. Soc. Phys. Rev. B* **1988**, *38*, 3433–3437.

(83)   Corradini, P. G.; Antolini, E.; Perez, J. Structural and Electrochemical Characterization of Carbon Supported Pt-Pr Catalysts for Direct Ethanol Fuel Cells Prepared Using a Modified Formic Acid Method in a CO Atmosphere. *Phys. Chem. Chem. Phys.* **2013**, *15*, 11730–11739.

(84)   Sunding, M. F.; Hadidi, K.; Diplas, S.; Løvvik, O. M.; Norby, T. E.; Gunnæs, A. E. XPS Characterisation of in Situ Treated Lanthanum Oxide and Hydroxide Using Tailored Charge Referencing and Peak Fitting Procedures. *J. Electron Spectros. Relat. Phenomena* **2011**, *184*, 399–409.

(85)   Zou, P.; Yao, M.; Chen, J.; Peng, Y.; Yao, X. Leakage Current and Dielectric Breakdown in Lanthanum Doped Amorphous Aluminum Oxide Films Prepared by Sol–Gel. *Ceram. Int.* **2016**, *42*, 4120–4125.

(86)   Maiti, K.; Fink, J.; de Jong, S.; Gorgoi, M.; Lin, C.; Raichle, M.; Hinkov, V.; Lambacher, M.; Erb, A.; Golden, M. S. Doping Dependence of the Chemical Potential and Surface Electronic Structure in YBa2Cu3O6+x and La2-XSrxCuO4 Using Hard x-Ray Photoemission Spectroscopy. *Phys. Rev. B* **2009**, *80*, 165132.

(87)   Rodrigues, A.; Bauer, S.; Baumbach, T. Effect of Post-Annealing on the Chemical State and Crystalline Structure of PLD Ba0.5Sr0.5TiO3 Films Analyzed by Combined Synchrotron X-Ray Diffraction and X-Ray Photoelectron Spectroscopy. *Ceram. Int.* **2018**, *44*, 16017–16024.

(88)   Cabrera-German, D.; Gomez-Sosa, G.; Herrera-Gomez, A. Accurate Peak Fitting and Subsequent Quantitative Composition Analysis of the Spectrum of Co 2p Obtained with Al Kα Radiation: I: Cobalt Spinel. *Surf. Interface Anal.* **2016**, *48*, 252–256.

(89)   Zhu, J.; Li, H.; Zhong, L.; Xiao, P.; Xu, X.; Yang, X.; Zhao, Z.; Li, J. Perovskite Oxides: Preparation, Characterizations, and Applications in Heterogeneous Catalysis. *ACS Catal.* **2014**, *4*, 2917–2940.

(90)   Hutchings, G. J.; Bartley, J. K.; Lopez-Sanchez, J. A.; Carley, A. F.; Rhodes, C.; Webster, J. M.; Gilbert, D. J.; Howdle, S. M.; Poliakoff, M.; Kiely, C. J.; Sajip, S.; Caldarelli, S.; Volta, J. C. Amorphous Vanadium Phosphate Catalysts from Supercritical Antisolvent Precipitation. *J. Catal.* **2001**, *197*, 232–235.

(91)   Kondrat, S. A.; Davies, T. E.; Zu, Z.; Boldrin, P.; Bartley, J. K.; Carley, A. F.; Taylor, S. H.; Rosseinsky, M. J.; Hutchings, G. J. The Effect of Heat Treatment on Phase Formation of Copper

Manganese Oxide: Influence on Catalytic Activity for Ambient Temperature Carbon Monoxide Oxidation. *J. Catal.* **2011**, *281*, 279–289.

(92)   Marin, R. P.; Kondrat, S. A.; Pinnell, R. K.; Davies, T. E.; Golunski, S.; Bartley, J. K.; Hutchings, G. J.; Taylor, S. H. Green Preparation of Transition Metal Oxide Catalysts Using Supercritical CO2 Anti-Solvent Precipitation for the Total Oxidation of Propane. *Appl. Catal. B Environ.* **2013**, *140–141*, 671–679.

(93)   Puigdollers, A. R.; Schlexer, P.; Tosoni, S.; Pacchioni, G. Increasing Oxide Reducibility: The Role of Metal/Oxide Interfaces in the Formation of Oxygen Vacancies. *ACS Catal.* **2017**, *7*, 6493–6513.

(94)   Liu, L.; Zhou, F.; Wang, L.; Qi, X.; Shi, F.; Deng, Y. Low-Temperature CO Oxidation over Supported Pt, Pd Catalysts: Particular Role of FeOx Support for Oxygen Supply during Reactions. *J. Catal.* **2010**, *274*, 1–10.

(95)   Pan, K. L.; Yu, S. J.; Yan, S. Y.; Chang, M. B. Direct N2O Decomposition over La2NiO4-Based Perovskite-Type Oxides. *J. Air Waste Manag. Assoc.* **2014**, *64*, 1260–1269.

(96)   Zhao, Z.; Yang, X.; Wu, Y. Comparative Study of Nickel-Based Perovskite-like Mixed Oxide Catalysts for Direct Decomposition of NO. *Appl. Catal. B Environ.* **1996**, *8*, 281–297.

(97)   Dacquin, J. P.; Lancelot, C.; Dujardin, C.; Da Costa, P.; Djega-Mariadassou, G.; Beaunier, P.; Kaliaguine, S.; Vaudreuil, S.; Royer, S.; Granger, P. Influence of Preparation Methods of LaCoO3on the Catalytic Performances in the Decomposition of N2O. *Appl. Catal. B Environ.* **2009**, *91*, 596–604.

(98)   Bhavani, A. G.; Kim, W. Y.; Lee, J. S. Barium Substituted Lanthanum Manganite Perovskite for CO2 Reforming of Methane. *ACS Catal.* **2013**, *3*, 1537–1544.

(99)   Wu, Y.; Ni, X.; Beaurain, A.; Dujardin, C.; Granger, P. Stoichiometric and Non-Stoichiometric Perovskite-Based Catalysts: Consequences on Surface Properties and on Catalytic Performances in the Decomposition of N 2O from Nitric Acid Plants. *Appl. Catal. B Environ.* **2012**, *125*, 149–157.

(100)   Guesmi, H.; Berthomieu, D.; Kiwi-Minsker, L. Nitrous Oxide Decomposition on the Binuclear [Fe II (μ-O)(μ-OH)Fe II] Center in Fe-ZSM-5 Zeolite. *J. Phys. Chem. C* **2008**, *112*, 20319–20328.

(101)   Sang, C.; Kim, B. H.; Lund, C. R. F. Effect of NO upon N 2 O Decomposition over Fe/ZSM-5 with Low Iron Loading [†]. *J. Phys. Chem. B* **2005**, *109*, 2295–2301.

(102) Hansen, N.; Heyden, A.; Bell, A. T.; Keil, F. J. A Reaction Mechanism for the Nitrous Oxide Decomposition on Binuclear Oxygen Bridged Iron Sites in {Fe-ZSM-5}. *J. Phys. Chem. C* **2007**, *111*, 2092–2101.

(103) Bulushev, D. A.; Kiwi-minsker, L.; Renken, A. Dynamics of N 2 O Decomposition over Fe / ZSM-5 Catalysts : Effects Of. *Ind. Eng. Chem. Res.* **2004**, *211*, 2004.

(104) Sun, K.; Xia, H.; Hensen, E.; Santen, R. van; Li, C. Chemistry of N2O Decomposition on Active Sites with Different Nature: Effect of High Temperature Treatment of Fe/ZSM-5. *J. Catal.* **2006**, *238*, 186–195.

(105) Pirngruber, G. D. The Surface Chemistry of N2O Decomposition on Iron Containing Zeolites (I). *J. Catal.* **2003**, *219*, 456–463.

(106) R.Wood, B.; Reimer, J. A.; Bell, A. T. Studies of N2O Adsorption and Decomposition on Fe–ZSM-5. *J. Catal.* **2002**, *209*, 151–158.

(107) Sadykov, V. A.; Bulgakov, N. N.; Muzykantov, V. S.; Kuznetsova, T. G.; Alikina, G. M.; Lukashevich, A. I.; Potapova, Y. V.; Rogov, V. A.; Burgina, E. B.; Zaikovskii, V. I.; Moroz, E. M.; Litvak, G. S.; Yakovleva, I. S.; Isupova, L. A.; Zyryanov, V. V.; Kemnitz, E.; Neophytides, S. Mobility and Reactivity of the Surface and Lattice Oxygen of Some Complex Oxides with Perovskite Structure. In *Mixed Ionic Electronic Conducting Perovskites for Advanced Energy Systems*; Springer Netherlands: Dordrecht, 2004; pp 53–74.

(108) Gu, Q.; Wang, L.; Wang, Y.; Li, X. Effect of Praseodymium Substitution on La1-XPrxMnO3 (X=0–0.4)Perovskites and Catalytic Activity for NO Oxidation. *J. Phys. Chem. Solids* **2019**, *133*, 52–58.

(109) Osazuwa, O. U.; Cheng, C. K. Catalytic Conversion of Methane and Carbon Dioxide (Greenhouse Gases) into Syngas over Samarium-Cobalt-Trioxides Perovskite Catalyst. *J. Clean. Prod.* **2017**, *148*, 202–211.

(110) Fierro, J. L. G.; Peña, M. A.; González Tejuca, L. An XPS and Reduction Study of PrCoO3. *J. Mater. Sci.* **1988**, *23*, 1018–1023.

(111) Alifanti, M.; Bueno, G.; Parvulescu, V.; Parvulescu, V. I.; Cortés Corberán, V. Oxidation of Ethane on High Specific Surface SmCoO3 and PrCoO3 Perovskites. *Catal. Today* **2009**, *143*, 309–314.

(112) Ayodele, B. V.; Khan, M. R.; Cheng, C. K. Greenhouse Gases Mitigation by CO2 Reforming of Methane to Hydrogen-Rich Syngas Using Praseodymium Oxide Supported Cobalt Catalyst. *Clean Technol. Environ. Policy* **2017**, *19*, 795–807.

(113) Klebanoff, L. E.; Van Campen, D. G.; Pouliot, R. J. Spin-Resolved and High-Energy-Resolution XPS Studies of Cobalt Metal and a Cobalt Magnetic Glass. *Phys. Rev. B* **1994**, *49*, 2047–2057.

(114) Mekki, A.; Salim, M. XPS Study of Transition Metal Doped Silicate Glasses. *J. Electron Spectros. Relat. Phenomena* **1999**, *101*, 227–232.

(115) Hassel, M.; Freund, H.-J. High Resolution XPS Study of a Thin CoO(111) Film Grown on Co(0001). *Surf. Sci. Spectra* **1996**, *4*, 273–278.

(116) Cordier, P. *Dislocations in Minerals*; 2004.